SCIENCE CHINA
Information Sciences

• RESEARCH PAPER •

November 2025, Vol. 68, Iss. 11, 212303:1–212303:14
https://doi.org/10.1007/s11432-025-4469-1

High-resolution ISAR imaging based on robust gamma process Laplace network

Yujie ZHANG[1], Xueru BAI[1*] & Feng ZHOU[2]

[1]*National Key Laboratory of Radar Signal Processing, Xidian University, Xi'an 710071, China*
[2]*School of Aerospace Science and Technology, Xidian University, Xi'an 710126, China*

Received 14 January 2025/Revised 26 March 2025/Accepted 4 June 2025/Published online 22 September 2025

Abstract Achieving robust well-focused ISAR imaging in diverse observation scenarios is critical for practical applications. However, the available iterative algorithms require elaborate parameter tuning, while model-driven networks necessitate model retraining for different observation conditions, limiting their practicality. To tackle these issues, this paper proposes a novel sparse Bayesian learning network, dubbed robust gamma process Laplace network (RGaPLN), for ISAR imaging in complex environments. Firstly, our previously proposed 2D inverse-free gamma process Laplace (2D-IFGaPL) algorithm is unfolded into a deep network to eliminate the need for parameter tuning. Then, a convolutional neural network (CNN) is integrated into the unfolded network to enhance robustness against variations in signal-to-noise ratio (SNR). Furthermore, a hypernetwork is designed to dynamically generate optimal parameters for different data missing rate (DMR), enabling ISAR imaging without model retraining under varying SNR and DMR conditions. Experimental results have demonstrated the effectiveness and superiority of the proposed method under various SNR and DMR conditions.

Keywords inverse synthetic aperture radar (ISAR) imaging, complex observation conditions, algorithm unfolding, sparse Bayesian learning (SBL), deep learning

Citation Zhang Y J, Bai X R, Zhou F. High-resolution ISAR imaging based on robust gamma process Laplace network. Sci China Inf Sci, 2025, 68(11): 212303, https://doi.org/10.1007/s11432-025-4469-1

1 Introduction

Due to the superior capabilities of high-resolution imaging under all-day and all-weather conditions, inverse synthetic aperture radar (ISAR) has been extensively used in space situational awareness and air surveillance [1–5]. Generally, ISAR achieves high range resolution by transmitting signals with large time-bandwidth product and pulse compression; and achieves high azimuth resolution through relative motion between the target and radar. Particularly, the relative motion consists of translational motion and rotational motion. The former destroys the coherence among echoes [6] and should be compensated [7], while the latter is beneficial for producing high azimuth resolution.

For ideal observation conditions such as high signal-to-noise ratio (SNR) and complete data, ISAR can obtain well-focused images through accurate translational motion compensation and conventional Fourier analysis techniques, i.e., the range Doppler (RD) algorithm. Unfortunately, the observation conditions in practice may become rather complex: (1) echoes reflected by long-distance, weak-scattering moving targets have low and time-varying SNR [8]; (2) jamming mitigation and ISAR resource scheduling lead to incomplete echoes [9] with changing data missing rate (DMR). Although the sparse signal reconstruction theory [10] has addressed the above issues to some extent, the existing methods require cumbersome parameter tuning to obtain well-focused images. Moreover, the optimal parameters vary with SNR and DMR, thereby necessitating parameter re-adjustment when the observation conditions change. Therefore, sophisticated methods should be designed to achieve robust ISAR imaging under complex observation conditions with varying SNR and DMR, in order to boost imaging performance and reduce both time and space complexity.

In recent years, extensive research has been focused on ISAR imaging under complex observation conditions based on sparse signal reconstruction [11–14]. These methods exploit the sparsity of ISAR

* Corresponding author (email: xrbai@xidian.edu.cn)

images, reformulate ISAR imaging as a sparse signal reconstruction problem, and then solve it through numerical optimization or sparse Bayesian learning (SBL) techniques. Specifically, the numerical optimization techniques impose sparsity constraint on the ISAR image using l_0 norm or l_1 norm, and typical methods include orthogonal matching pursuit (OMP) [15] and alternating direction method of multipliers (ADMM) [16,17]. Although these methods are easy to implement, determining the optimal regularization parameters is still an open problem. Furthermore, they suffer from rapid performance degradation under low SNR and high DMR conditions. On the other hand, by introducing sparse priors and establishing probabilistic models, the SBL methods fully exploit the statistical characteristics of the ISAR image, and then infer the posterior distribution utilizing Bayesian inference techniques, thereby achieving accurate ISAR imaging under low SNR and high DMR conditions [18,19]. Among the available sparse priors, the nonparametric priors, e.g., the beta process prior [20] and the gamma process-Laplace prior [21], have demonstrated superior performance due to their flexibility. Despite their satisfying imaging performance, the SBL methods typically involve numerous matrix inversions and require careful tuning of model parameters, leading to low imaging efficiency. Although some methods have been proposed to eliminate the matrix inversion by relaxing the lower bound [22, 23], the optimal choice of the model parameters remains an important problem.

The rapid advancement of deep learning in the past few years has spurred significant interest in utilizing deep networks for high-resolution ISAR imaging [24–26]. These methods can be broadly classified into data-driven and model-driven approaches. The data-driven methods utilize the superior nonlinear mapping abilities of deep networks to directly learn the relationship between radar echoes and ISAR images [27]. However, these methods lack interpretability and require massive training data, hindering their practical application. In contrast, the model-driven methods truncate and unfold iterative algorithms into limited-layer networks and learn the algorithm parameters through end-to-end training, thereby achieving higher reconstruction accuracy than the iterative algorithms [28, 29]. Typical methods include ISTA-net [30, 31], ADMM-net [32, 33], and AMP-net [34]. Notably, these methods possess several advantages: (1) the algorithm parameters are learned from data, avoiding the time-consuming manual parameter tuning process in traditional iterative algorithms; (2) the unfolded networks naturally inherit domain knowledge from iterative algorithms, providing stronger interpretability than data-driven methods; (3) the number of learnable parameters is limited in the unfolded networks, thus requiring less training data than data-driven methods. Despite their excellent performance, available model-driven methods should be trained under fixed SNR and DMR conditions due to their limited network capacity, and retraining is required when the SNR and DMR of test samples deviate from those of the training samples, thereby leading to low robustness and high complexity.

It should be noted that, the available model-driven ISAR imaging networks rely on numerical optimization techniques and fail to exploit statistical characteristics of the target and the environment, thereby possessing unsatisfying performance. On the contrary, designing effective SBL methods and unfolding them into deep networks may boost the imaging performance under low SNR and high DMR conditions.

In view of this, this paper proposes a novel ISAR imaging method based on robust gamma process Laplace network (RGaPLN), which combines SBL and deep networks to achieve robust ISAR imaging in complex observation conditions with varying SNR and DMR. The main contributions are summarized as follows.

(1) A novel ISAR imaging method based on RGaPLN is proposed, which effectively addresses the issue of parameter tuning in conventional iterative algorithms and achieves robust ISAR imaging under different SNR and DMR conditions without retraining.

(2) A deep unfolded network is proposed, which is constructed by unfolding the 2D-IFGaPL algorithm. Particularly, with the detailed analysis of the update mechanism of the iterative algorithm, a convolutional neural network (CNN) is integrated into the unfolded network to enhance robustness against SNR variation.

(3) A hypernetwork, composed of convolutional and fully-connected layers, is designed to dynamically generate the algorithm parameters according to the DMR, thereby improving the adaptability to DMR variation and eliminating model retraining.

(4) Monte Carlo simulations demonstrate that the proposed method outperforms the available methods in reconstruction accuracy. In addition, imaging results of both simulated and measured data further indicate that the proposed method can obtain well-focused images for echoes with various SNR and DMR.

The rest of this paper is organized as follows. In Section 2, we construct the ISAR sparse observation model and establish a probabilistic model based on the gamma process-Laplace prior. In Section 3, we

introduce the proposed ISAR imaging method based on RGaPLN in detail. In Section 4, we validate the effectiveness of the proposed method through Monte Carlo simulations and imaging experiments using simulated and measured data. Finally, we conclude the paper in Section 5.

2 Modelling

2.1 Signal modelling

After translational motion compensation, the rotational motion of a target can be represented by a turntable model. For the linear frequency modulated (LFM) waveform, the radar echoes after dechirping satisfy [21]

$$s\left(f_r,t_m\right)=\sum_{p=1}^{P}\sigma_p\mathrm{rect}\left(\frac{f_r}{B}\right)\exp\left(-\mathrm{j}\frac{4\pi}{c}\left(f_r+f_c\right)R_p\left(t_m\right)\right)+n\left(t_m\right), \tag{1}$$

where f_r, t_m, p, σ_p, B, c, f_c, $R_p\left(t_m\right)$ and $n\left(t_m\right)$ represent the range frequency, the slow time, the index of scattering centers, the backscattering coefficient of the pth scattering center, the signal bandwidth, the light speed, the carrier frequency, the instantaneous slant range of the pth scattering center and the additive noise, respectively. Particularly, for a steadily moving target with a small accumulation angle, $R_p\left(t_m\right)$ can be approximated by

$$R_p\left(t_m\right)=x_p\omega t_m+y_p \tag{2}$$

with x_p and y_p denote the azimuth and range coordinates of the pth scattering center, respectively, and ω is the rotation speed. Substituting (2) into (1), we obtain

$$s\left(f_r,t_m\right)=\sum_{p=1}^{P}\sigma_p\mathrm{rect}\left(\frac{f_r}{B}\right)\exp\left(-\mathrm{j}\frac{4\pi}{c}\left(f_r+f_c\right)\left(x_p\omega t_m+y_p\right)\right)+n\left(t_m\right). \tag{3}$$

By substituting $f_r=n\Delta f$ and $t_m=m/\mathrm{PRF}$ into (3), we can obtain the discretized echoes as

$$s\left(n,m\right)=\sum_{p=1}^{P}\sigma_p\mathrm{rect}\left(\frac{n\Delta f}{B}\right)\exp\left(-\mathrm{j}\frac{4\pi}{c}\left(n\Delta f+f_c\right)\left(x_p\omega\frac{m}{\mathrm{PRF}}+y_p\right)\right)+n\left(m\right), \tag{4}$$

where $n\in[1,N_r]$ is the range samples index, $m\in[1,N_a]$ is the echoes index, $\Delta f=B/N_r$ is the range frequency interval, PRF is the pulse repetition frequency.

Subsequently, Eq. (4) can be reformulated as

$$\mathbf{S}=\mathbf{F}_r\mathbf{X}\mathbf{F}_a+\mathbf{N}, \tag{5}$$

where $\mathbf{S}\in\mathbb{C}^{N_r\times N_a}$ represents the radar echoes matrix, $\mathbf{F}_r\in\mathbb{C}^{N_r\times J}$ represents the range observation dictionary, $\mathbf{X}\in\mathbb{C}^{J\times Q}$ represents the unknown ISAR image, $\mathbf{F}_a\in\mathbb{C}^{Q\times N_a}$ represents the azimuth observation dictionary, and $\mathbf{N}\in\mathbb{C}^{N_r\times N_a}$ represents the noise matrix.

2.2 Probabilistic modelling

Since the distribution of the scattering centers of the ISAR targets usually exhibits strong sparsity, we exploit such characteristic and establish a probabilistic model by introducing the gamma process-Laplace nonparametric prior [21] to $\mathbf{X}$, which is defined as follows:

$$p\left(\mathbf{S}|\mathbf{X},\xi\right)=\prod_{n=1}^{N_r}\prod_{m=1}^{N_a}\mathrm{CN}\left(S_{nm}|\mathbf{F}_{rn\cdot}\mathbf{X}\mathbf{F}_{a\cdot m},\xi^{-1}\right), \tag{6}$$

$$p\left(\xi\right)=\mathrm{Gam}\left(\xi|a,b\right), \tag{7}$$

$$p\left(\mathbf{X}|\mathbf{\Gamma}\right)=\prod_{j=1}^{J}\prod_{q=1}^{Q}\mathrm{Lap}\left(X_{jq}|\Gamma_{jq}\right), \tag{8}$$

$$p\left(\Gamma_{jq}\right)=\mathrm{Gam}\left(\Gamma_{jq}|1/JQ\ ,d\right), \tag{9}$$

where $\mathbf{F}_{rn\cdot}$ is the nth row of $\mathbf{F}_r$, $\mathbf{F}_{a\cdot m}$ is the mth column of $\mathbf{F}_a$, ξ is the noise precision, $\mathrm{CN}(\cdot|\mu,\sigma)$ represents the complex Gaussian distribution with mean μ and covariance σ, $\mathrm{Gam}(\cdot)$ represents the gamma distribution, $\mathrm{Lap}(\cdot)$ is the Laplace distribution, and a, b and d represent the model hyperparameters. Particularly, as $JQ \to \infty$, the random measure $G = \sum_{j=1}^{J}\sum_{q=1}^{Q}\Gamma_{jq}\delta_{\mathbf{F}_{r\cdot j}\mathbf{F}_{aq\cdot}}$ becomes the gamma process [35], thus providing great flexibility in data description.

3 Model solving

In this section, we first briefly introduce the 2D-IFGaPL algorithm. On this basis, the RGaPLN is constructed through deep unfolding of the 2D-IFGaPL algorithm and integrating a hypernetwork to achieve robust high-resolution imaging. Below, we will introduce the proposed method in detail.

3.1 2D-IFGaPL

Since the posterior distribution of the probabilistic model is intractable, our previously proposed 2D-IFGaPL algorithm [21] solves the probabilistic model using the expectation maximization (EM) technique [36]. Firstly, a vectorized signal model is constructed to facilitate inference, i.e.,

$$\mathbf{s} = \mathbf{\Phi}\mathbf{x} + \mathbf{n}, \tag{10}$$

where $\mathbf{s}$, $\mathbf{x}$ and $\mathbf{n}$ represent the vector form of $\mathbf{S}$, $\mathbf{X}$ and $\mathbf{N}$, which are obtained by stacking the corresponding matrix along the column; $\mathbf{\Phi} = \mathbf{F}_a^{\mathrm{T}} \otimes \mathbf{F}_r$, with $\otimes$ denoting the Kronecker product.

To eliminate the heavy computational burden induced by matrix inversion in the M step, the 2D-IFGaPL algorithm relaxes the EM lower bound $\mathcal{L}(\mathbf{x})$ as

$$\begin{aligned}\mathcal{L}(\mathbf{x}) =& \mathbb{E}_{q(\mathbf{x},\xi,\lambda)}\left[\ln p(\mathbf{s},\mathbf{x},\xi,\gamma)\right]\\ \geqslant& -\mathbb{E}_{q(\xi)}\left[\xi\right]\left(\|\mathbf{s}-\mathbf{\Phi}\boldsymbol{\delta}\|_2^2 + 2\,\mathrm{Re}\left(\left(\mathbf{x}-\boldsymbol{\delta}\right)^{\mathrm{H}}\mathbf{\Phi}^{\mathrm{H}}\left(\mathbf{\Phi}\boldsymbol{\delta}-\mathbf{s}\right)\right) + L\|\mathbf{x}-\boldsymbol{\delta}\|_2^2\right)\\ &-2\sum_{i=1}^{JQ}\mathbb{E}_{q(\gamma)}\left[1/\gamma_i\right]|x_i| + \mathrm{const},\end{aligned} \tag{11}$$

where $\mathbb{E}_{q(\cdot)}[\cdot]$ represents the expectation defined by $\mathbb{E}_q[x] = \int xq(x)\,\mathrm{d}x$, q represents the posterior distribution, $\mathrm{Re}(\cdot)$ represents taking the real part, and $(\cdot)^{\mathrm{H}}$ represents the conjugate transpose. Then, maximizing the relaxed EM lower bound in the M-step yields the inverse-free update formula of $\mathbf{x}$.

Finally, by applying the property of the Kronecker product, we can obtain the iterative algorithm in matrix form as follows:

$$\begin{aligned}\mathbf{X}^{(k+1)} =& \mathbb{E}_{q(\xi)}[\xi]^{(k)}\left(L\mathbf{X}^{(k)} - \mathbf{F}_r^{\mathrm{H}}\left(\mathbf{F}_r\mathbf{X}^{(k)}\mathbf{F}_a - \mathbf{S}\right)\mathbf{F}_a^{\mathrm{H}}\right)\\ &\oslash\left(L_{q(\xi)}[\xi]^{(k)}\mathbf{I} + \mathbb{E}_{q(\mathbf{\Gamma})}[\mathbf{\Gamma}]^{(k)} \oslash \left|\mathbf{X}^{(k)}\right|\right),\\ \mathbb{E}_{q(\xi)}[\xi]^{(k+1)} =& \frac{a+N_rN_a}{b+\left\|\mathbf{S}-\mathbf{F}_r\mathbf{X}^{(k+1)}\mathbf{F}_a\right\|_F^2},\\ \mathbb{E}_{q(\mathbf{\Gamma})}\left[\mathbf{\Gamma}_{jq}\right] =& \frac{\sqrt{d}\mathcal{K}_{c-3}\left(\sqrt{8d\left|\mathbf{X}_{jq}^{(k+1)}\right|}\right)}{\sqrt{2\left|\mathbf{X}_{jq}^{(k+1)}\right|}\mathcal{K}_{c-2}\left(\sqrt{8d\left|\mathbf{X}_{jq}^{(k+1)}\right|}\right)},\end{aligned} \tag{12}$$

where k is the iteration number, $\oslash$ denotes the element-wise division, $|\cdot|$ denotes taking the modulus, $\|\cdot\|_F$ denotes the Frobenius norm, and $\mathcal{K}_c(\cdot)$ denotes the modified Bessel function of the second kind.

3.2 RGaPLN

Although the 2D-IFGaPL algorithm can achieve accurate reconstruction of the ISAR image, two issues still need to be addressed: (1) under different SNR and DMR conditions, the algorithm requires fine-tuning of parameters d and L to obtain satisfying imaging results, which is usually cumbersome and

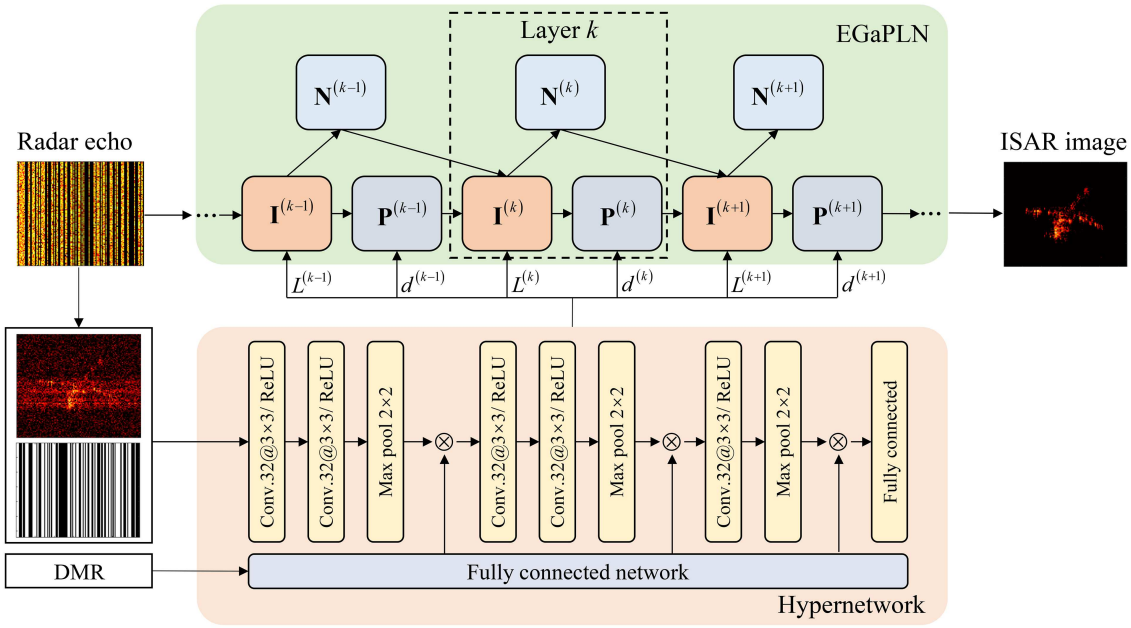

Figure 1 (Color online) Structure of RGaPLN. There are three modules in the kth layer of EGaPLN, i.e., image reconstruction module (**I**), noise precision estimation module (**N**) and image precision estimation module (**P**), corresponding to the iterative steps in (12).

time-consuming; (2) the parameters for all iterative steps remain fixed and lack flexibility, which may degrade imaging performance. To address these issues, this paper proposes RGaPLN, which learns model parameters of each layer separately, eliminating the issue of manual parameter tuning and enhancing network flexibility. Additionally, to tackle the issue of network retraining due to limited capacity, it integrates a CNN into the unfolded network to gain robustness to varying SNR, and further integrates a hypernetwork to gain robustness to varying DMR.

Figure 1 depicts the network structure of the RGaPLN. It is observed that the RGaPLN consists of two parts: the enhanced gamma process Laplace network (EGaPLN) and the hypernetwork. The latter generates parameters of each layer, while the former adopts these parameters to reconstruct the ISAR image.

3.2.1 *EGaPLN*

The EGaPLN is constructed by unfolding the 2D-IFGaPL algorithm. Specifically, the EGaPLN has K layers, with each layer containing three modules: the image reconstruction module, the noise precision estimation module, and the image precision estimation module. Since each module is constructed according to the corresponding iteration formula, the network possesses great interpretability and ensures the ISAR image $\mathbf{X}$ being appropriately updated throughout the forward process. Below, we will introduce the EGaPLN in detail.

(1) Image reconstruction module (**I**). This module reconstructs the ISAR image according to the iteration formula of $\mathbf{X}$ in (12). For the kth module $\mathbf{I}^{(k)}$, it accepts four inputs, i.e., $\mathbb{E}_{q(\xi)}[\xi]^{(k-1)}$, $L^{(k)}$, $\mathbf{X}^{(k-1)}$ and $\mathbb{E}_{q(\mathbf{\Gamma})}[\mathbf{\Gamma}]^{(k-1)}$, and outputs $\mathbf{X}^{(k)}$, i.e.,

$$\begin{aligned}\mathbf{X}^{(k)} =& \mathbb{E}_{q(\xi)}[\xi]^{(k-1)}\left(L^{(k)}\mathbf{X}^{(k-1)} - \mathbf{F}_r^{\mathrm{H}}\left(\mathbf{F}_r\mathbf{X}^{(k-1)}\mathbf{F}_a - \mathbf{S}\right)\mathbf{F}_a^{\mathrm{H}}\right)\\ &\oslash\left(L^{(k)}\mathbb{E}_{q(\xi)}[\xi]^{(k-1)}\mathbf{I} + \mathbb{E}_{q(\mathbf{\Gamma})}[\mathbf{\Gamma}]^{(k-1)} \oslash \left|\mathbf{X}^{(k-1)}\right|\right),\end{aligned} \tag{13}$$

where $L^{(k)}$ denotes the learnable parameter of the kth layer. In the first layer (i.e., $k=1$), $\mathbf{X}^{(1)} = \mathbf{F}_r^{\mathrm{H}}\mathbf{S}\mathbf{F}_a^{\mathrm{H}}$.

(2) Noise precision estimation module (**N**). This module estimates the posterior expectation of the noise precision according to the iteration formula of $\mathbb{E}_{q(\xi)}[\xi]$ in (12). For the kth module $\mathbf{N}^{(k)}$, it accepts

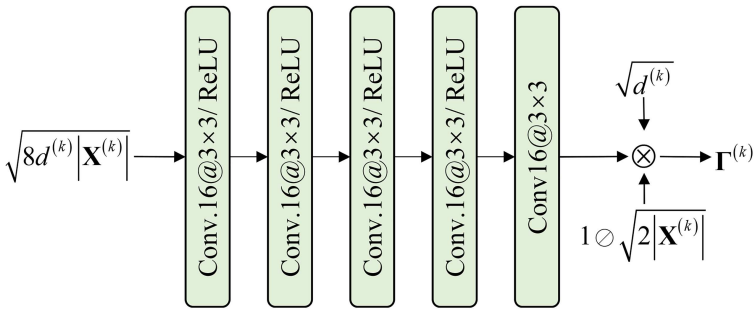

Figure 2 (Color online) Structure of the image precision estimation module.

input $\mathbf{X}^{(k)}$ and outputs $\mathbb{E}_{q(\xi)}[\xi]^{(k)}$ as follows:

$$\mathbb{E}_{q(\xi)}[\xi]^{(k)} = \frac{a + N_r N_a}{b + \left\|\mathbf{S} - \mathbf{F}_r \mathbf{X}^{(k)} \mathbf{F}_a\right\|_F^2}. \tag{14}$$

(3) Image precision estimation module (**P**). This module estimates the posterior expectation of image precision $\mathbb{E}_{q(\mathbf{\Gamma})}[\mathbf{\Gamma}]$. Although this module can be designed by strictly unfolding the update formula of $\mathbb{E}_{q(\mathbf{\Gamma})}[\mathbf{\Gamma}]$ in (12), the corresponding learnable parameters are quite sensitive to SNR variations, thereby necessitating network retraining under different SNR conditions.

To address this problem, we reformulate the update formula of $\mathbf{X}$ in (12) as follows and scrutinize the role of $\mathbb{E}_{q(\mathbf{\Gamma})}[\mathbf{\Gamma}]$, i.e.,

$$\mathbf{X}^{(k)} = \left(\mathbf{X}^{(k-1)} - \mathbf{F}_r^{\mathrm{H}} \left(\mathbf{F}_r \mathbf{X}^{(k-1)} \mathbf{F}_a - \mathbf{S}\right) \mathbf{F}_a^{\mathrm{H}} \Big/ L\right) \oslash \left(\mathbf{1} + \left(\mathbb{E}_{q(\mathbf{\Gamma})}[\mathbf{\Gamma}] \oslash \left|\mathbf{X}^{(k-1)}\right|\right) \Big/ \left(L \mathbb{E}_{q(\xi)}[\xi]\right)\right), \tag{15}$$

where $\mathbf{1}$ denotes the matrix with all ones. Then, the first term can be expressed in vector form as

$$\mathrm{vec}\left(\mathbf{X}^{(k-1)} - \mathbf{F}_r^{\mathrm{H}} \left(\mathbf{F}_r \mathbf{X}^{(k-1)} \mathbf{F}_a - \mathbf{S}\right) \mathbf{F}_a^{\mathrm{H}} \Big/ L\right) = \left(\mathbf{x}^{(k-1)} - \mathbf{\Phi}^{\mathrm{H}} \left(\mathbf{\Phi} \mathbf{x}^{(k-1)} - \mathbf{s}\right) \Big/ L\right). \tag{16}$$

Considering $\nabla_{\mathbf{x}} \|\mathbf{s} - \mathbf{\Phi}\mathbf{x}\|_2^2 = 2\mathbf{\Phi}^{\mathrm{H}} (\mathbf{\Phi}\mathbf{x} - \mathbf{s})$, Eq. (16) can be rewritten as

$$\mathrm{vec}\left(\mathbf{X}^{(k-1)} - \mathbf{F}_r^{\mathrm{H}} \left(\mathbf{F}_r \mathbf{X}^{(k-1)} \mathbf{F}_a - \mathbf{S}\right) \mathbf{F}_a^{\mathrm{H}} \Big/ L\right) = \mathbf{x}^{(k-1)} - \nabla_{\mathbf{x}^{(k-1)}} \left\|\mathbf{s} - \mathbf{\Phi}\mathbf{x}^{(k-1)}\right\|_2^2 \Big/ 2L, \tag{17}$$

which is indeed the gradient descent with a step size of $1/2L$ and ensures that the reconstruction result minimizes the negative log-likelihood, i.e., $\|\mathbf{s} - \mathbf{\Phi}\mathbf{x}\|_2^2$. In addition, the second term in (15) acts as a mask to adjust the gradient descent result. Particularly, L and $\mathbb{E}_{q(\xi)}[\xi]$ serve as scaling factors which change the overall amplitude of $\mathbf{X}$; while $\mathbb{E}_{q(\mathbf{\Gamma})}[\mathbf{\Gamma}]$ assigns values separately to each entry of $\mathbf{X}$ and enhances the reconstruction flexibility. It should be noted that in order to adapt to different SNR, the magnitude of $\mathbb{E}_{q(\mathbf{\Gamma})}[\mathbf{\Gamma}]$ should be adjusted elaborately and manually in the 2D-IFGaPL algorithm. Moreover, the primary unfolding network can only obtain $\mathbb{E}_{q(\mathbf{\Gamma})}[\mathbf{\Gamma}]$ suitable for a specific SNR, thereby still requiring model retraining for different SNR. To achieve noise robustness, however, the magnitude of $\mathbb{E}_{q(\mathbf{\Gamma})}[\mathbf{\Gamma}]$ should be able to adjust adaptively according to the varying SNR without parameter tuning or model retraining.

In view of this, we design a CNN to estimate $\mathbb{E}_{q(\mathbf{\Gamma})}[\mathbf{\Gamma}]$. For the kth module $\mathbf{P}^{(k)}$, it accepts two inputs $d^{(k)}$ and $\mathbf{X}^{(k)}$, and outputs $\mathbb{E}_{q(\mathbf{\Gamma})}[\mathbf{\Gamma}]^{(k)}$, i.e.,

$$\mathbb{E}_{q(\mathbf{\Gamma})}[\mathbf{\Gamma}]^{(k)} = \sqrt{d^{(k)}} f_\theta \left(\sqrt{8d^{(k)} \left|\mathbf{X}^{(k)}\right|}\right) \oslash \sqrt{2\left|\mathbf{X}^{(k)}\right|}, \tag{18}$$

where $d^{(k)}$ denotes the learnable parameter of the kth layer, and f_θ denotes a CNN with parameter set θ. As shown in Figure 2, the CNN in the image precision estimation module consists of five convolution layers with a convolution kernel size of 3×3. Particularly, to reduce the number of network parameters, such a structure is shared among layers.

It should be noted that the parameters d and L in EGaPLN are not shared among layers to improve the model flexibility. Additionally, the integrated CNN in EGaPLN generates suitable masks adaptively for echoes with different SNR, thereby improving model robustness and reconstruction accuracy. The experimental results presented in Section 4 will further demonstrate such superiority.

3.2.2 *Hypernetwork*

Although the EGaPLN can achieve noise robustness owing to the learnable image precision estimation module, it fails to adjust parameters automatically according to the varying DMR. To address this issue, we design and integrate a CNN-based hypernetwork to EGaPLN and obtain RGaPLN.

Specifically, the hypernetwork accepts the DMR and the channel-concatenated image of $\mathbf{X}^{(1)}$ and DMPI (i.e., the image that describes the data missing pattern), extracts features from echoes with different DMR, and generates the corresponding optimal parameters $\{\mathbf{d}, \mathbf{L}\}$, i.e.,

$$\{\mathbf{d}, \mathbf{L}\} = \mathcal{H}_{\psi}\left(\mathbf{X}^{(1)}, \mathrm{DMPI}, \mathrm{DMR}\right), \tag{19}$$

where $\mathbf{d} = \left(d^{(1)}, \ldots, d^{(K)}\right)$ and $\mathbf{L} = \left(L^{(1)}, \ldots, L^{(k)}\right)$ are the algorithm parameters, $\mathcal{H}_{\psi}(\cdot)$ is the hypernetwork with parameter set ψ, and $\mathbf{X}^{(1)} = \mathbf{F}_r^{\mathrm{H}}\mathbf{S}\mathbf{F}_a^{\mathrm{H}}$ is the initialized image.

As shown in Figure 1, the hypernetwork includes five convolutional layers, three pooling layers, and one fully connected (FC) layer. Each convolutional layer utilizes a 3×3 kernel with 32 channels and rectified linear unit (ReLU) activation. The pooling layers utilize a 2×2 kernel with a stride of 2 for down-sampling. The FC layer converts the resulting 32 1×1 feature into a vector with dimension $2K$, i.e., $[\mathbf{d}, \mathbf{L}]$. In addition, the FC network consists of a single FC layer that maps the scalar DMR to a 32-dimensional vector, which is then adopted to weight the activated features in the CNN, thereby enabling automatic adaptation to varying DMR conditions.

4 Experiments

In this section, we begin by introducing the dataset and the training details. Next, we evaluate and compare the performance of EGaPLN and RGaPLN with available methods using Monte Carlo experiments. Finally, we illustrate the effectiveness of EGaPLN and RGaPLN by presenting the ISAR images of both simulated and measured data under various SNR and DMR conditions. All experiments were performed on an Intel Xeon Silver 4114 CPU and an NVIDIA GeForce RTX 3090 GPU.

4.1 Dataset

Given the difficulty in acquiring sufficient labeled measured data, we generate point simulated dataset for network training. The simulated dataset contains 900 samples, with 800 used for training and 100 reserved for testing. Each sample contains 300 randomly distributed scattering centers, the dimension of the label image $\mathbf{X}$ is 128×128. Particularly, to mimic various target shapes and structures, the distributions of scattering centers amplitudes include Chi-squared, Gaussian, exponential, and gamma distributions, respectively, while their locations obey uniform or Gaussian distributions. Typical label images of the simulated dataset are shown in Figure 3. Then, echoes are generated according to $\mathbf{S} = \mathbf{F}_r\mathbf{X}\mathbf{F}_a + \mathbf{N}$, with Gaussian noise added, resulting in SNR that is uniformly distributed in $[-1, 11]$ dB. In addition, Figure 4 presents an example of the DMPI with DMR of 50%, where the white blocks represent the available echoes and the black blocks represent the missing echoes.

4.2 Training details

In this paper, the loss functions of EGaPLN and RGaPLN are defined as follows:

$$\mathrm{Loss} = \sum_{l=1}^{N_t} \left\| \hat{\mathbf{X}}_l - \mathbf{X}_l^{gt} \right\|_F^2, \tag{20}$$

where $\hat{\mathbf{X}}_l$ and $\mathbf{X}_l^{gt}$ are the estimated image and the label image of the lth sample, respectively, and N_t denotes the batch size. For both EGaPLN and RGaPLN, the parameters a and b are set to 10^{-4}. For EGaPLN, the parameters d and L in each layer are initialized as 5 and 0.5, respectively. The EGaPLN is trained separately with a fixed DMR. In contrast, the RGaPLN is trained by samples with DMR uniformly distributed in [25%, 75%]. Moreover, to achieve the optimal imaging performance, the training parameters of EGaPLN and RGaPLN are set as specified in Table 1. Particularly, their training epochs are set to different values to ensure network convergence while preventing overfitting.

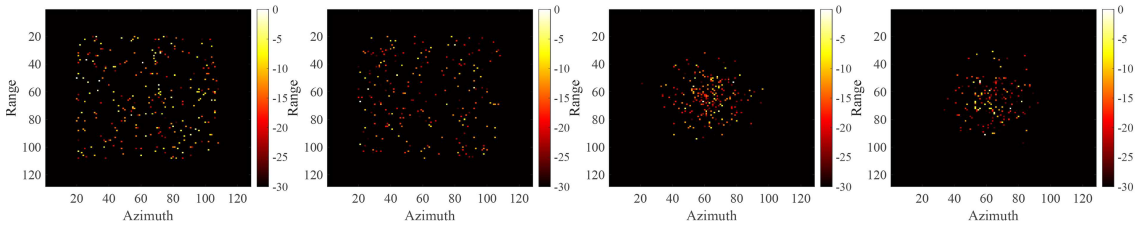

Figure 3 (Color online) Typical label images of the simulated data.

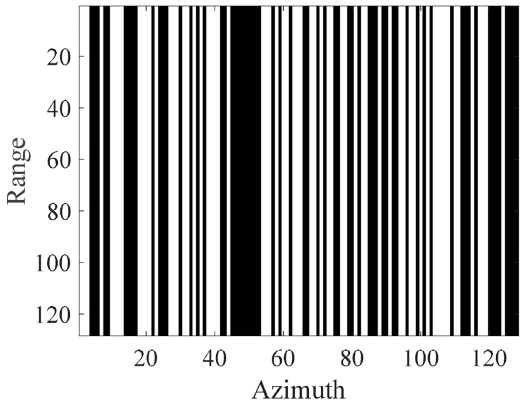

Figure 4 Example of the DMPI with DMR of 50%.

Table 1 Training parameters of EGaPLN and RGaPLN.

	Learning rate	Batch size	Training epoch	Optimizer
EGaPLN	2×10^{-4}	8	400	Adam
RGaPLN	5×10^{-5}	1	200	Adam

4.3 Monte Carlo experiments

4.3.1 *Layer number determination*

The reconstruction accuracy of the unfolded network is strongly dependent on the number of layers. Therefore, we first determine the layer number of EGaPLN and RGaPLN using the testing data. The number of layers varies from 6 to 14 with an interval of 2, and the SNR varies from 0 to 10 dB in steps of 2 dB. For each SNR and layer number, 100 experiments are carried out, and the normalized average root mean square error (RMSE) is presented in Figure 5. Specifically, the normalized RMSE is defined as follows:

$$\text{Normlized RMSE} = \frac{\sqrt{\hat{\mathbf{X}} - \mathbf{X}^{gt}}}{JQ} \Bigg/ \left\| \frac{\sqrt{\hat{\mathbf{X}} - \mathbf{X}^{gt}}}{JQ} \right\|_F. \tag{21}$$

As shown in Figure 5, as the number of layers increases, the RMSE of both EGaPLN and RGaPLN decreases firstly and then becomes stable when the number of layers is greater than 12. Therefore, we select the layer number of 12 for both EGaPLN and RGaPLN in subsequent experiments to achieve a balance between the computational efficiency and the reconstruction accuracy.

4.3.2 *Reconstruction performance evaluation*

In this part, we compare the performance of EGaPLN and RGaPLN with 2D-IFGaPL [19], 2D-ADN [31], HCM-AMPN [32] and primary GaPLN (PGaPLN) through Monte Carlo simulation. Particularly, the PGaPLN is obtained by directly unfolding the 2D-IFGaPL algorithm without integrating the CNN in the image precision estimation module. Moreover, due to their limited network capacity, 2D-ADN, HCM-AMPN and PGaPLN cannot achieve robust imaging under varying observation conditions. Therefore, they should be trained separately utilizing samples with fixed SNR and DMR to achieve the optimal imaging performance.

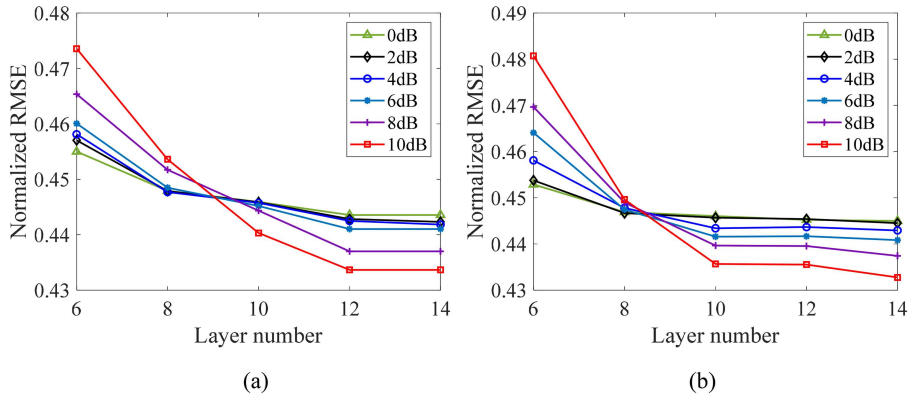

Figure 5 (Color online) Variation of the normalized RMSE with layer number for different methods. (a) EGaPLN; (b) RGaPLN.

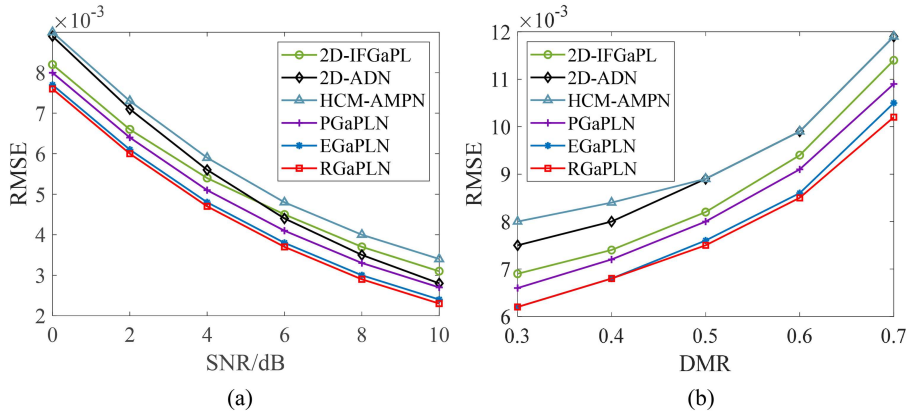

Figure 6 (Color online) Monte Carlo results of different methods. (a) The average RMSE under different SNR conditions; (b) the average RMSE under different DMR conditions.

Firstly, the reconstruction performance under different SNR conditions is evaluated. The DMR is set to 50%, and the SNR varies from 0 to 10 dB in steps of 2 dB. For each SNR, 100 independent experiments are conducted, and the average RMSE is depicted in Figure 6(a). It is observed that RGaPLN can obtain the lowest RMSE under different SNR conditions, indicating its superior reconstruction accuracy. Moreover, EGaPLN can achieve higher reconstruction accuracy than PGaPLN under different SNR conditions without retraining, demonstrating the effectiveness of the CNN incorporated in EGaPLN.

Furthermore, we evaluate the reconstruction performance of EGaPLN and RGaPLN under different DMR conditions. The SNR is fixed at 0 dB, while the DMR ranges from 30% to 70% with an interval of 10%. For each DMR, 100 experiments are performed and the average RMSE is depicted in Figure 6(b). It is observed that RGaPLN still obtains the highest reconstruction accuracy under different DMR conditions.

4.4 Imaging results with electromagnetic simulated data

We utilize the electromagnetic simulated data from the F-16 airplane to validate the proposed method in this section. The radar parameters are $f_c = 16$ GHz and $B = 2$ GHz. The full-aperture echoes comprise 128 pulses, with each pulse having 128 samples. For the full-aperture and noise-free data, the ISAR image obtained using the RD algorithm is presented in Figure 7.

The ISAR imaging is performed with SNR of 0 and 5 dB, and DMR of 30%, 50%, and 70%. Figures 8 and 9 present the ISAR images obtained by different methods. It can be seen that the 2D-ADN and HCM-AMPN methods suffer from background noise and excessively sparse scattering centers, compromising the completeness of the target structure. In contrast, since the proposed EGaPLN and RGaPLN methods can exploit the statistical characteristics of both the target and the environment, they produce well-focused images with cleaner background and more complete target structure under different SNR and DMR conditions.

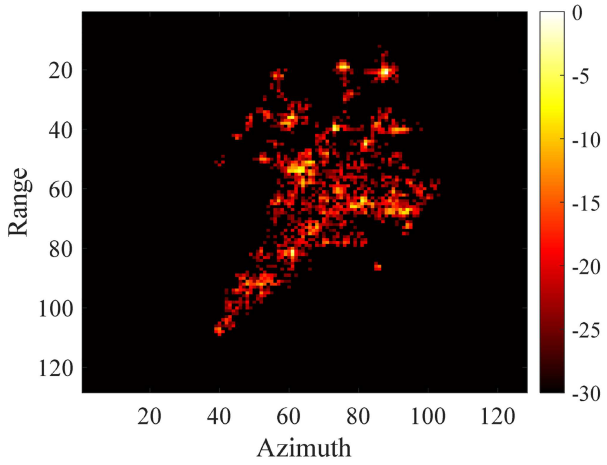

Figure 7 (Color online) RD image of electromagnetic simulated data of the F-16 airplane with full-aperture, noise-free data.

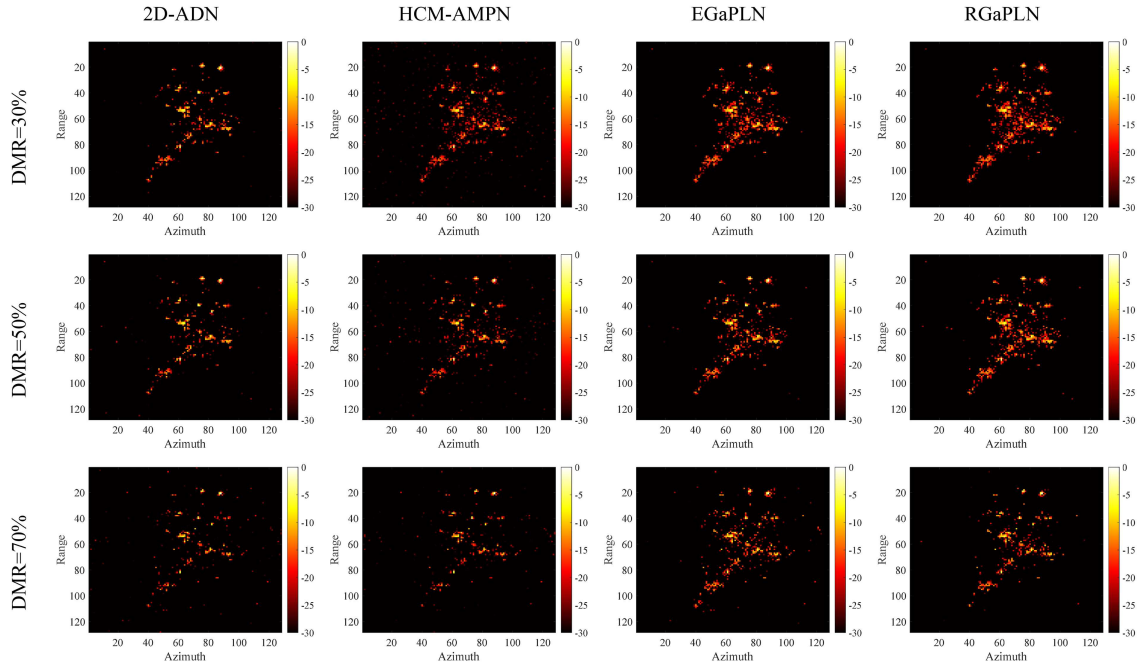

Figure 8 (Color online) Imaging results of electromagnetic simulated data of the F-16 airplane for SNR of 0 dB.

For a quantitative comparison, the peak signal-to-noise ratio (PSNR) and the structural similarity index measure (SSIM) between the imaging results and the RD image presented in Figure 7 are calculated. As shown in Table 2, the proposed EGaPLN and RGaPLN methods achieve higher PSNR and SSIM compared to the available methods under different observation conditions, with RGaPLN, enhanced by the hypernetwork, outperforming EGaPLN.

4.5 Imaging results with measured data

To further validate the effectiveness of the proposed method, we perform the imaging experiments with measured data of the Yak-42 airplane. The RD image of the full-aperture data is shown in Figure 10.

Similarly, imaging experiments are carried out with SNR of 0 and 5 dB, and DMR of 30%, 50%, and 70%. The imaging results are illustrated in Figures 11 and 12. As can be seen, imaging results of 2D-ADN and HCM-AMPN suffer from background noise and incomplete target structure, especially when SNR is 0 dB and DMR is 70%. In contrast, EGaPLN and RGaPLN can still achieve well-focused imaging with clearer background and better structural completeness under varying conditions. Furthermore, Table 3 lists the corresponding SSIM and PSNR between the imaging results and the corresponding RD image,

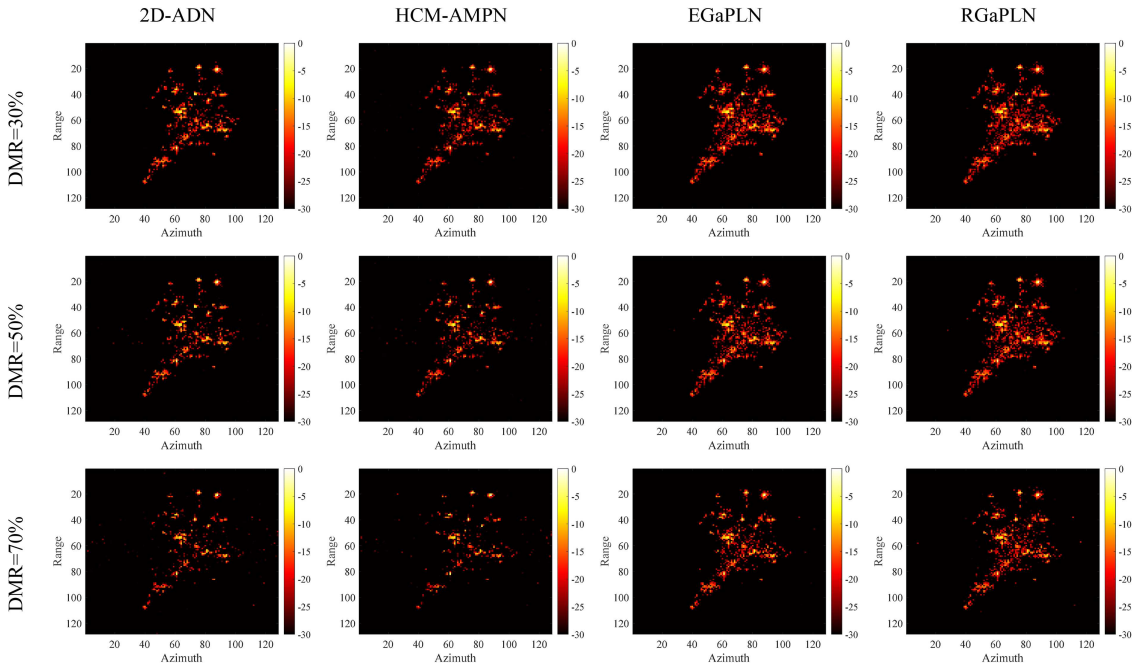

Figure 9 (Color online) Imaging results of electromagnetic simulated data of the F-16 airplane for SNR of 5 dB.

Table 2 Numerical results of electromagnetic simulated data of the F-16 airplane. Bold values indicate the optimal results.

SNR	DMR	Evaluation index	2D-ADN	HCM-AMPN	EGaPLN	RGaPLN
0 dB	30%	PSNR	34.5669	35.2380	36.7730	**37.0269**
		SSIM	0.8969	0.8354	0.9387	**0.9435**
	50%	PSNR	33.6246	33.9168	34.6842	**35.1908**
		SSIM	0.8774	0.8595	0.9068	**0.9186**
	70%	PSNR	32.4549	32.4111	32.9055	**32.9734**
		SSIM	0.8368	0.8402	0.8750	**0.8792**
5 dB	30%	PSNR	38.4132	39.0805	42.7479	**42.8692**
		SSIM	0.9552	0.9397	0.9854	**0.9861**
	50%	PSNR	36.3104	36.6003	39.3371	**40.1949**
		SSIM	0.9235	0.9683	**0.9764**	0.9737
	70%	PSNR	34.1466	33.6738	35.5841	**35.7879**
		SSIM	0.8762	0.8727	0.9294	**0.9317**

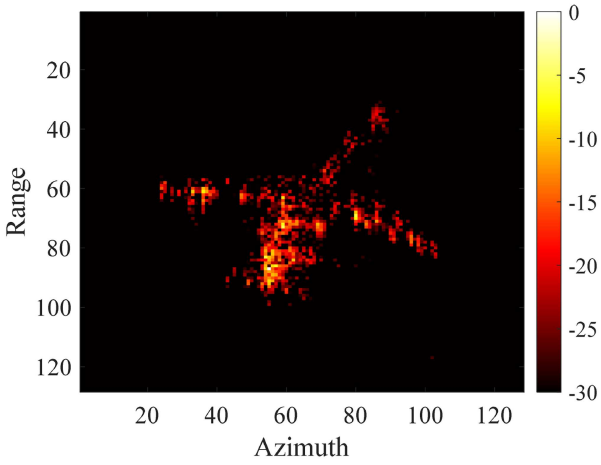

Figure 10 (Color online) RD image of measured data of the Yak-42 airplane with full-aperture data.

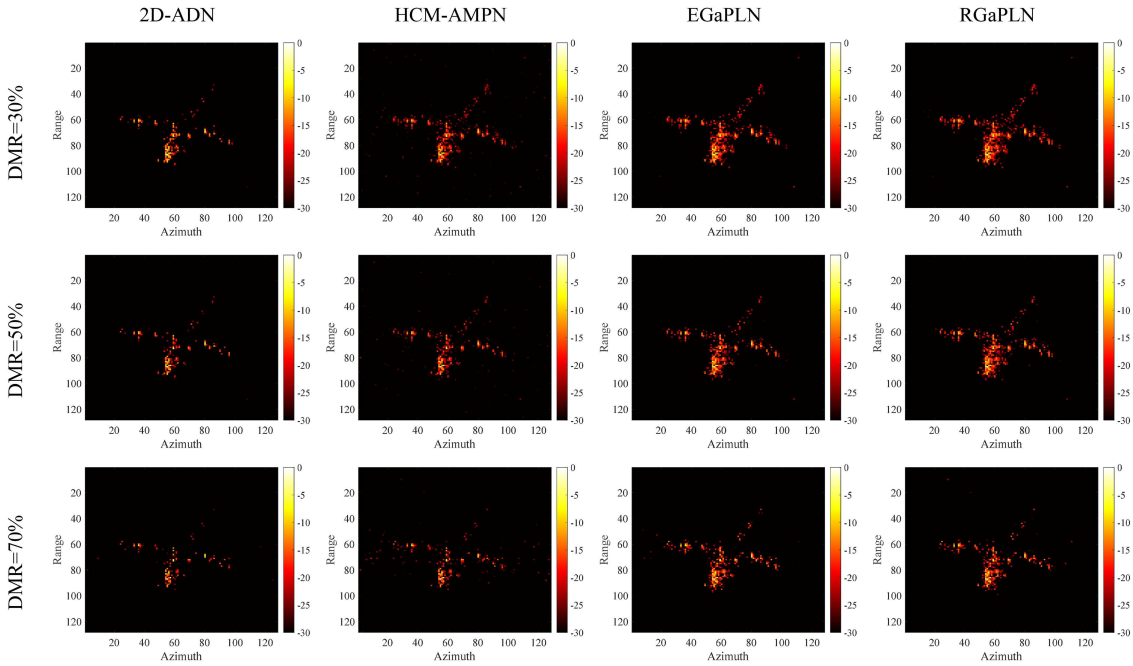

Figure 11 (Color online) Imaging results of measured data of the Yak-42 airplane for SNR of 0 dB.

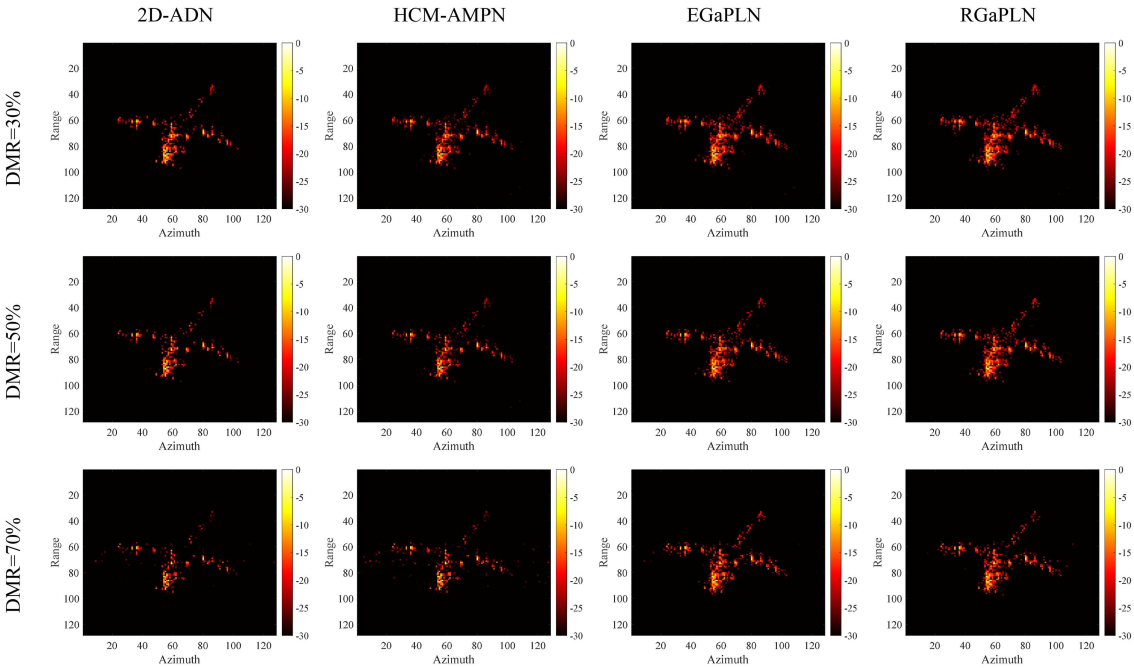

Figure 12 (Color online) Imaging results of measured data of the Yak-42 airplane for SNR of 5 dB.

where the proposed methods achieve higher SSIM and PSNR, further demonstrating their superiority.

5 Conclusion

To achieve robust ISAR imaging in varying observation environments, this paper proposes an SBL network called RGaPLN. Firstly, the 2D-IFGaPL algorithm is unfolded into a deep network. Then, a CNN is incorporated into the unfolded network to increase the robustness against the SNR variation. On this basis, a hypernetwork is further incorporated to generate algorithm parameters dynamically according to DMR, thereby achieving robust high-resolution imaging under various SNR and DMR conditions

Table 3 Numerical results of measured data of the Yak-42 airplane. Bold values indicate the optimal results.

SNR	DMR	Evaluation index	2D-ADN	HCM-AMPN	EGaPLN	RGaPLN
0 dB	30%	PSNR	37.2183	38.7350	41.0074	**41.2900**
		SSIM	0.9265	0.8979	0.9635	**0.9670**
	50%	PSNR	36.2296	37.3932	38.6509	**38.9834**
		SSIM	0.9200	0.9175	0.9464	**0.9515**
	70%	PSNR	35.0028	35.4947	36.8829	**36.9030**
		SSIM	0.9086	0.9042	**0.9343**	0.9330
5 dB	30%	PSNR	40.7104	42.8980	46.2290	**46.3290**
		SSIM	0.9598	0.9650	0.9879	**0.9890**
	50%	PSNR	38.8328	40.1703	42.3064	**43.4822**
		SSIM	0.9484	0.9575	0.9755	**0.9807**
	70%	PSNR	36.7746	36.8230	38.9765	**39.0406**
		SSIM	0.9294	0.9246	0.9574	**0.9575**

without model retraining. The experimental results have validated the effectiveness and robustness of the proposed method under different SNR and DMR conditions.

Acknowledgements This work was supported by National Natural Science Foundation of China (Grant Nos. 62425113, 62131020).

References

1 Bai X, Zhang Y, Liu S. High-resolution radar imaging of off-grid maneuvering targets based on parametric sparse Bayesian learning. IEEE Trans Geosci Remote Sens, 2022, 60: 1–11
2 Wang H, Chen Y, Zhang Y, et al. High-resolution ISAR imaging method for maneuvering targets based on a hybrid transformer. IEEE Trans Antennas Propagat, 2023, 71: 8250–8265
3 Chen C, Xu Z, Tian S. An efficient sparse aperture ISAR imaging framework for maneuvering targets. IEEE Trans Antennas Propagat, 2024, 72: 1873–1886
4 Chen X, Ye C, Wang Y, et al. Imaging algorithm for inverse synthetic aperture radar in condition of non-uniform data rate. IEEE Trans Comput Imag, 2023, 9: 396–408
5 Chen Z Y, Li Y H, Hu C, et al. Repeat-pass space-surface bistatic SAR tomography: accurate imaging and first experiment. Sci China Inf Sci, 2024, 67: 192304
6 Chen V C, Martorella M. Inverse Synthetic Aperture Radar Imaging: Principles, Algorithms and Applications. London: IET Digital Library, 2014
7 Liu F, Huang D, Guo X, et al. Translational motion compensation for maneuvering target echoes with sparse aperture based on dimension compressed optimization. IEEE Trans Geosci Remote Sens, 2022, 60: 1–16
8 Ding Z, Zhang G, Zhang T, et al. An improved parametric translational motion compensation algorithm for targets with complex motion under low signal-to-noise ratios. IEEE Trans Geosci Remote Sens, 2022, 60: 1–14
9 Xu G, Zhang B, Chen J, et al. Structured low-rank and sparse method for ISAR imaging with 2-D compressive sampling. IEEE Trans Geosci Remote Sens, 2022, 60: 1–14
10 Li H, Dai F, Zhao Q, et al. Non-uniform compressive sensing imaging based on image saliency. Chin J Elect, 2023, 32: 159–165
11 Xu G, Zhang B, Chen J, et al. Sparse inverse synthetic aperture radar imaging using structured low-rank method. IEEE Trans Geosci Remote Sens, 2022, 60: 1–12
12 Bai X, Wang G, Liu S, et al. High-resolution radar imaging in low SNR environments based on expectation propagation. IEEE Trans Geosci Remote Sens, 2021, 59: 1275–1284
13 Xu G, Zhang B, Yu H, et al. Sparse synthetic aperture radar imaging from compressed sensing and machine learning: theories, applications, and trends. IEEE Geosci Remote Sens Mag, 2022, 10: 32–69
14 Zhang S, Liu Y, Li X, et al. Joint sparse aperture ISAR autofocusing and scaling via modified Newton method-based variational Bayesian inference. IEEE Trans Geosci Remote Sens, 2019, 57: 4857–4869
15 Bae J, Kang B, Lee S, et al. Bistatic ISAR image reconstruction using sparse-recovery interpolation of missing data. IEEE Trans Aerosp Electron Syst, 2016, 52: 1155–1167
16 Hashempour H R. Sparsity-driven ISAR imaging based on two-dimensional ADMM. IEEE Sens J, 2020, 20: 13349–13356
17 Xu Z Q, Zhang B C, Li G Z, et al. Analysis of phase preservation and interferometric offset test in sparse SAR imaging. Sci China Inf Sci, 2024, 67: 122303
18 Xiong S, Li K, Wang H, et al. Sparse aperture high-resolution RID ISAR imaging of maneuvering target based on parametric efficient sparse Bayesian learning. IEEE Geosci Remote Sens Lett, 2024, 21: 1–5
19 Wang Y, Dai F, Liu Q, et al. 2-D joint high-resolution ISAR imaging with random missing observations via cyclic displacement decomposition-based efficient SBL. IEEE Trans Geosci Remote Sens, 2024, 62: 1–19
20 Zhou F, Tian X, Wang Y, et al. High-resolution ISAR imaging under low SNR with sparse stepped-frequency chirp signals. IEEE Trans Geosci Remote Sens, 2021, 59: 8338–8348
21 Zhang Y, Bai X, Liu S, et al. Joint translational motion compensation and high-resolution ISAR imaging based on sparse Bayesian learning. IEEE Trans Comput Imag, 2024. doi: 10.1109/TCI.2024.3468014
22 Worley B. Scalable mean-field sparse Bayesian learning. IEEE Trans Signal Process, 2019, 67: 6314–6326
23 Wang Y, Zhang Y, Bai X. High-resolution ISAR imaging with SSFCS based on nonparametric Bayesian learning and genetic algorithm. IEEE Trans Geosci Remote Sens, 2023, 61: 1–12
24 Chen M, Xia J Y, Liu T, et al. An integrated network for SA-ISAR image processing with adaptive denoising and super-resolution modules. IEEE Geosci Remote Sens Lett, 2024, 21: 1–5
25 Wang L, Wang L, Conde M H, et al. A fast total-variation driven network for sparse aperture ISAR imaging. Digital Signal Process, 2024, 151: 104515
26 Mai Y, Zhang S, Jiang W, et al. ISAR imaging of target exhibiting micro-motion with sparse aperture via model-driven deep network. IEEE Trans Geosci Remote Sens, 2022, 60: 1–12
27 Gao J, Deng B, Qin Y, et al. Enhanced radar imaging using a complex-valued convolutional neural network. IEEE Geosci Remote Sens Lett, 2019, 16: 35–39

28 Monga V, Li Y, Eldar Y C. Algorithm unrolling: interpretable, efficient deep learning for signal and image processing. IEEE Signal Process Mag, 2021, 38: 18–44
29 Zhang J, Chen B, Xiong R, et al. Physics-inspired compressive sensing: beyond deep unrolling. IEEE Signal Process Mag, 2023, 40: 58–72
30 Li H, Xu J, Song H, et al. PIN: sparse aperture ISAR imaging via self-supervised learning. IEEE Geosci Remote Sens Lett, 2024, 21: 1–5
31 Zhang H, Ni J, Xiong S, et al. SR-ISTA-Net: sparse representation-based deep learning approach for SAR imaging. IEEE Geosci Remote Sens Lett, 2022, 19: 1–5
32 Li R, Zhang S, Zhang C, et al. Deep learning approach for sparse aperture ISAR imaging and autofocusing based on complex-valued ADMM-Net. IEEE Sens J, 2021, 21: 3437–3451
33 Li X, Bai X, Zhou F. High-resolution ISAR imaging and autofocusing via 2D-ADMM-Net. Remote Sens, 2021, 13: 2326
34 Liang J, Wei S, Wang M, et al. Sparsity-driven ISAR imaging via hierarchical channel-mixed framework. IEEE Sens J, 2021, 21: 19222–19235
35 Roychowdhury R, Kulis B. Gamma processes, stick-breaking, and variational inference. In: Proceedings of the 18th International Conference on Artificial Intelligence and Statistics, San Diego, 2015. 800–808
36 Bishop M C. Pattern Recognition and Machine Learning. New York: Springer-Verlag, 2006